JACS
JOURNAL OF THE AMERICAN CHEMICAL SOCIETY
Article
Cite This: J. Am. Chem. Soc. 2017, 139, 16894-16902
pubs.acs.org/JACS

Reaction Coordinate Leading to H_2 Production in [FeFe]-Hydrogenase Identified by Nuclear Resonance Vibrational Spectroscopy and Density Functional Theory

Vladimir Pelmenschikov,[†,#] James A. Birrell,[‡,#] Cindy C. Pham,[§,#] Nakul Mishra,[§] Hongxin Wang,[§] Constanze Sommer,[‡] Edward Reijerse,[‡] Casseday P. Richers,[∥] Kenji Tamasaku,[⊥] Yoshitaka Yoda,[⊥] Thomas B. Rauchfuss,[∥] Wolfgang Lubitz,[‡] and Stephen P. Cramer*[,§]

[†]Institut für Chemie, Technische Universität Berlin, Strasse des 17 Juni 135, 10623 Berlin, Germany
[‡]Max-Planck-Institut für Chemische Energiekonversion, Stiftstrasse 34-36, 45470 Mülheim an der Ruhr, Germany
[§]Department of Chemistry, University of California, Davis, One Shields Avenue, Davis, California 95616, United States
[∥]School of Chemical Sciences, University of Illinois, 600 S. Mathews Avenue, Urbana, Illinois 61801, United States
[⊥]JASRI, Spring-8, 1-1-1 Kouto, Mikazuki-cho, Sayo-gun, Hyogo 679-5198, Japan

Supporting Information

ABSTRACT: [FeFe]-hydrogenases are metalloenzymes that reversibly reduce protons to molecular hydrogen at exceptionally high rates. We have characterized the catalytically competent hydride state (H_{hyd}) in the [FeFe]-hydrogenases from both *Chlamydomonas reinhardtii* and *Desulfovibrio desulfuricans* using ^{57}Fe nuclear resonance vibrational spectroscopy (NRVS) and density functional theory (DFT). H/D exchange identified two Fe−H bending modes originating from the binuclear iron cofactor. DFT calculations show that these spectral features result from an iron-bound terminal hydride, and the Fe−H vibrational frequencies being highly dependent on interactions between the amine base of the catalytic cofactor with both hydride and the conserved cysteine terminating the proton transfer chain to the active site. The results indicate that H_{hyd} is the catalytic state one step prior to H_2 formation. The observed vibrational spectrum, therefore, provides mechanistic insight into the reaction coordinate for H_2 bond formation by [FeFe]-hydrogenases.

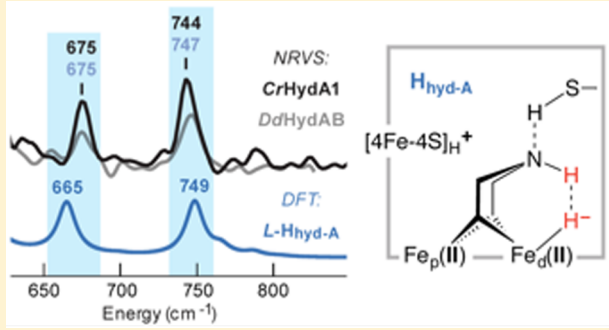

INTRODUCTION

Hydrogenases are enzymes that catalyze the reversible oxidation of molecular hydrogen and reduction of protons with high turnover frequencies under physiological conditions.[1,2] The [FeFe]-hydrogenases exhibit exceptional activity in both catalytic directions (>10 000 s^{-1} for *Dd*HydAB),[3] in part due to the unique structure of their active site cofactor. The active site of [FeFe]-hydrogenase, the "H-cluster",[1,2] consists of covalently linked binuclear $[2Fe]_H$ and iron−sulfur $[4Fe\text{-}4S]_H$ subclusters (Figure 1). The Fe_p and Fe_d sites of $[2Fe]_H$, respectively proximal and distal to $[4Fe\text{-}4S]_H$, are bridged by a CO ligand and an azadithiolate (ADT) cofactor, the latter also providing the nitrogen base of the frustrated Lewis pair crucial to H_2 conversion processes.[4−6] Fe_d, the site at which hydrogen binds, is the Lewis acid.[7,8] Many previous experimental and theoretical studies[9−12] implicate a $Fe_d{-}H_h{\cdots}H_A{-}N_{ADT}$ species as the key intermediate leading to H−H bond formation (Figure 1A). Despite its mechanistic importance, however, experimental characterization of such H···H interactions in the enzyme has not been available so far. Here, we show that under reducing conditions at low pH, the [FeFe]-hydrogenases from *Chlamydomonas reinhardtii* (*Cr*HydA1) and *Desulfovibrio desulfuricans* (*Dd*HydAB) both exhibit species with these key $Fe_d{-}H_h{\cdots}H_A{-}N_{ADT}$ interactions. These turnover conditions give high steady state levels of the terminal hydride bound state, H_{hyd}, by maximizing the rate of electron and proton transfer to the hydrogenase, such that the last step in hydrogen formation becomes rate limiting.

The ADT entity is situated at the terminus of a proton transfer pathway (Figure 1B). Protons are relayed to the active site from the protein surface via conserved residues (Glu144/159, Ser189/198, Glu141/156, and finally Cys169/178 respectively in *Cr*HydA1/*Dd*HydAB, here and below).[15,16] The proton transfer chain is conserved in both algal and bacterial [FeFe]-hydrogenases.[16] In contrast, the electron transport chains, containing accessory Fe−S clusters leading to $[4Fe\text{-}4S]_H$, vary significantly between organisms. For example, *Cr*HydA1 lacks accessory clusters altogether, while *Dd*HydAB contains two additional [4Fe-4S] clusters, and the

Received: September 12, 2017
Published: October 20, 2017

DOI: 10.1021/jacs.7b09751
J. Am. Chem. Soc. 2017, 139, 16894−16902

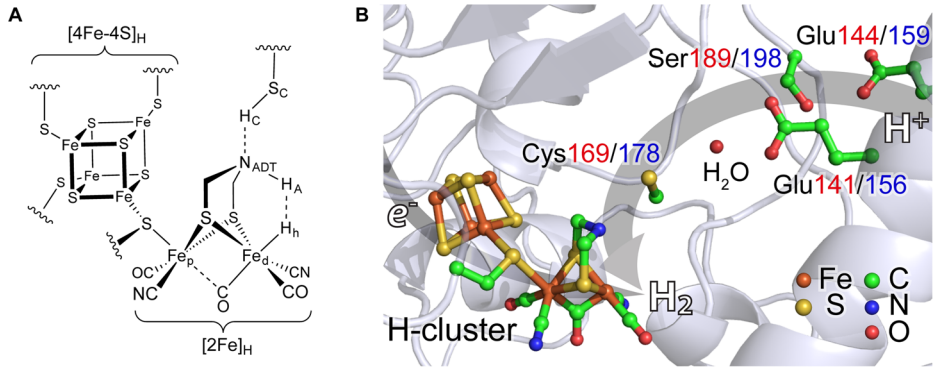

Figure 1. (A) Schematic illustration of the [FeFe]-hydrogenase H-cluster proposed for the H_{hyd} state. The hydride H_h at the iron site of the $[2Fe]_H$ subcluster Fe_d, distal to $[4Fe\text{-}4S]_H$, interacts with the "Axial" proton H_A of the ADT bridgehead nitrogen N_{ADT}. The cysteine, shown here as $-S_C-H_C$, terminates the proton supply chain and is in contact with N_{ADT}. (B) The H-cluster and its protein environment based on the crystal structure (1HFE).[13,14] Proposed proton (H^+) and electron (e^-) transfer pathways are shown in semitransparent gray arrows. Red and blue numbers correspond to the amino acid residues in *Cr*HydA1 and *Dd*HydAB, respectively.

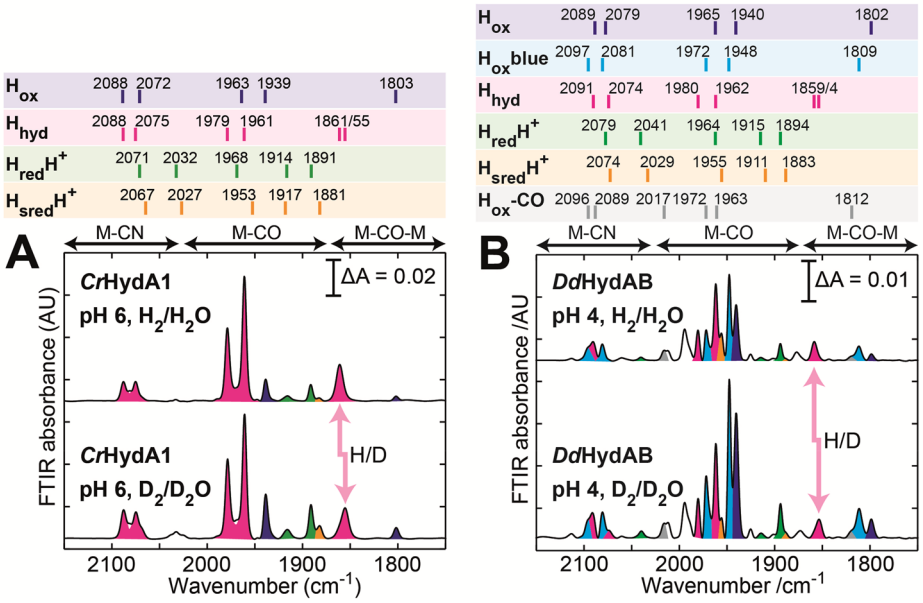

Figure 2. FT-IR spectra of the H_{hyd} state. Samples (10 μL) of 3–5 mM $[2^{57}Fe]_H$-*Cr*HydA1 at pH 6 (A) and 2–4 mM $[2^{57}Fe]_H$-*Dd*HydAB at pH 4 (B) were reduced with 100 mM sodium dithionite and transferred to the FT-IR cells. The samples were prepared either in H_2O under a 2% H_2 atmosphere (upper spectra) or in D_2O under a 2% D_2 atmosphere (lower spectra). Spectra were recorded within 5 min after the initial sample reduction. The peaks are shaded to indicate from which state they derive: H_{ox} (purple), H_{ox}blue (blue), H_{hyd} (pink), $H_{red}H^+$ (green), $H_{sred}H^+$ (orange), H_{ox}-CO (gray).

bidirectional hydrogenase from *Clostridium pasteurianum* (*Cp*HydA1) contains one [2Fe-2S] and three [4Fe-4S] clusters.

The thiol of Cys169/178 interacts via hydrogen bonding with the bridgehead N_{ADT} nitrogen of the ADT cofactor. Exchanging this cysteine for another amino acid can abolish or severely reduce the activity of [FeFe]-hydrogenases, as seen with the C299S variant of *Cp*HydA1,[16,17] and the C169A and C169S variants of *Cr*HydA1,[7,17] whereas C298D of hydrogenase from *Clostridium acetobutylicum* (*Ca*HydA) retains significant activity.[18] Modification of the proton transfer pathway by artificial maturation with complexes that substitute the −NH− ADT bridgehead with −O− (ODT) or $-CH_2-$ (PDT) also causes nearly complete loss of activity.[1,19]

Along with decreased activity, modification of the proton transfer pathway can stabilize states that are otherwise elusive, including some with unusual IR signatures now assigned as H_{hyd}.[7,17] The H_{hyd} state is thought to feature a reduced $[4Fe\text{-}4S]_H^+$ subcluster and a homovalent $Fe_p(II)Fe_d(II)$ binuclear $[2Fe]_H$ site, with a hydride H_h bound in the apical position on Fe_d.[20]

In previous work, we used nuclear resonance vibrational spectroscopy (NRVS) to examine the $[2^{57}Fe\text{-ODT}]_H$-*Cr*HydA1 H_{hyd} species.[21] NRVS is a synchrotron-based X-ray technique that involves observation of vibrational sidebands that occur in combination with nuclear transitions.[22−24] ^{57}Fe NRVS is particularly useful for vibrational analysis of Fe-containing enzymes because it is only sensitive to normal modes with ^{57}Fe motion. Using the recently developed method of artificial maturation of [FeFe]-hydrogenase with $[2^{57}Fe]_H$-labeling makes the technique completely selective for the normal modes of the subcluster.[25−27] For the $[2^{57}Fe\text{-ODT}]_H$-*Cr*HydA1 H_{hyd} samples, under H_2/H_2O conditions, Fe−H features were observed at 670 and 727 cm^{-1} (Figure S3) and rationalized by density functional theory (DFT) calculations as

DOI: 10.1021/jacs.7b09751
J. Am. Chem. Soc. 2017, 139, 16894−16902

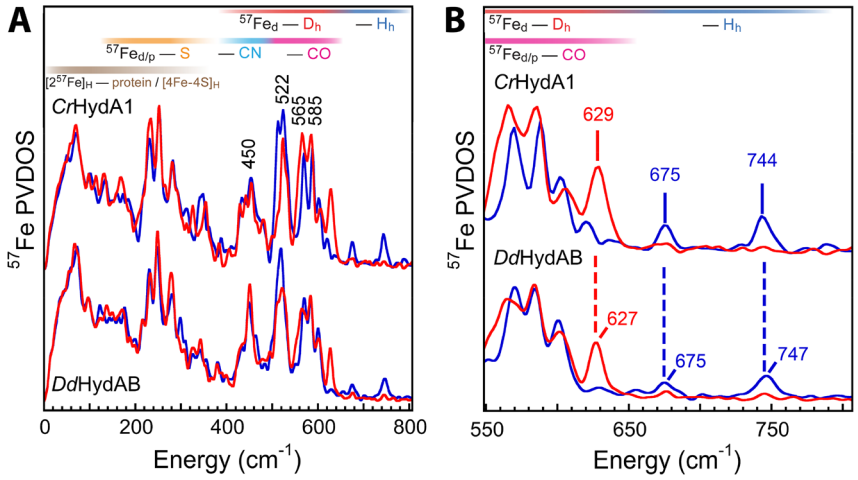

Figure 3. NRVS spectra of [FeFe]-hydrogenases. (A) The overall NRVS for samples of $[2^{57}Fe]_H$-*Cr*HydA1 (top) and $[2^{57}Fe]_H$-*Dd*HydAB (bottom) prepared under H_2/H_2O (blue) and D_2/D_2O (red). (B) Expansion of the Fe−H/D region of the NRVS for the same samples. Numbers at the top indicate representative peak positions in H_2/H_2O (blue) and D_2/D_2O (red) samples.

terminal hydride Fe_d−H_h bending modes. The corresponding red-shifted Fe_d-D_h modes were associated with the perturbed $Fe_{d/p}$−CO bands at 625 and 564 cm^{-1} under D_2/D_2O conditions.[21] The Fe_d−H_h vibrations at 670 and 727 cm^{-1} were assigned, respectively, to H^- motion perpendicular to and within the approximate mirror symmetry plane of $[2Fe]_H$, which passes through Fe_p, Fe_d, and H_h ($Fe_pFe_dH_h$ plane). Here we focus on the NRVS spectra for the H_{hyd} species from *Cr*HydA1 and *Dd*HydAB artificially maturated with $[2^{57}Fe]_H$.

As we show in this report, the structure of the hydride state(s) in [FeFe]-hydrogenase is extremely sensitive to subtle effects that are not directly at the Fe_d−H_h center. These remote effects include hydrogen bonding between Fe_d−H_h and ADT and between ADT and Cys169/178, the very sites that were modified in previous studies that demonstrated the existence of iron hydrides.[21,28] The overarching question remains: in the absence of such perturbations, *what is the structure of an iron-hydride in hydrogenase under turnover conditions?* The present paper addresses this question.

RESULTS AND DISCUSSION

H_{hyd} State Accumulation. The H_{hyd} states of the catalytically active $[2^{57}Fe]_H$-*Cr*HydA1 and $[2^{57}Fe]_H$-*Dd*HydAB enzymes were stabilized at low pH values (pH 6 and pH 4, respectively) and with high concentrations of a low potential reductant (sodium dithionite).[29] These turnover conditions give high steady state levels of H_{hyd}, which we rationalize as follows. With such a high concentration of reductant, the rate of electron transfer to the hydrogenase is very high. Around neutral pH, proton transfer from the nitrogen base in the $H_{sred}H^+$ state is rate limiting. Protonation at low pH, of the amino acid residues in the proton transfer pathway, increases the rate of proton transfer from the nitrogen base to the open coordination site on Fe_d forming the H_{hyd} state. The rate limiting step then becomes the coupled electron/proton transfer leading to hydrogen formation. Also, under these conditions, an initial burst of hydrogen production saturates the sample with hydrogen, which can rebind to Fe_d in the oxidized state reforming the H_{hyd} state.

FTIR Spectroscopy. The FTIR spectra for the H_{hyd} state in both $[2^{57}Fe]_H$-*Cr*HydA1 and $[2^{57}Fe]_H$-*Dd*HydAB under H_2/H_2O and D_2/D_2O (Figure 2) are very similar to those observed for $[2^{57}Fe\text{-ODT}]_H$-*Cr*HydA1.[21] The characteristic red-shift of the bridging CO band due to H/D exchange is attributed to coupling between the bridging CO vibration and the Fe_d−H_h vibration.[21] The possibility that this shift is due to H/D exchange in hydrogen bonds to the bridging CO ligand can be excluded because hydrogen bonds to the bridging CO ligand are not indicated crystallographically.[14,30,31] The H_{hyd} state in $[2^{57}Fe]_H$-*Cr*HydA1 was formed in high stoichiometric yield (≈90%) and appeared to be very stable (Figure S1A). In *Dd*HydAB, however, lower stability of the H_{hyd} state (Figure S1B) due to the much higher activity of this enzyme (≈10 000 s^{-1} compared with ≈1000 s^{-1} for *Cr*HydA1) gave slightly lower yields (≈ 50%) of the H_{hyd} state.[32,33] The major impurities were the H_{ox} state and a protonated form of the H_{ox} state (termed H_{ox}-blue).[29,34] The Mössbauer (Figure S2A) and EPR (Figure S2B) spectra of *Cr*HydA1 in the H_{hyd} state under H_2/H_2O are very similar to those previously published for both wild type *Cr*HydA1 and the C169S mutant.[28]

NRVS Spectroscopy. NRVS spectra for the two [FeFe]-hydrogenases under H_2/H_2O and D_2/D_2O conditions are illustrated in Figure 3A. Features in the 150−400 cm^{-1} range are primarily due to Fe−S bending and stretching motions, and hence they are relatively unaffected by H vs D conditions. Bands near 450 cm^{-1} involve mostly Fe-CN motion. Strong bands between 500−600 cm^{-1} are modes mostly of Fe-CO bending and stretching character; although their profiles are similar under H vs D conditions, there are indeed subtle changes that derive from coupling with Fe−H/D motion.[21]

Distinct evidence for the presence of an Fe−H/D bond comes in the higher frequency region between ≈620−750 cm^{-1} (Figure 3B). In both H_2/H_2O samples there are bands at 675 and 744/747 cm^{-1}, which are replaced by a feature at 629/627 cm^{-1} in the D_2/D_2O samples. The high frequencies and isotope sensitivity help assign these features as hydride/deuteride bands. The close similarity of the Fe−H/D modes in the two different enzymes suggests nearly identical structures for the H_{hyd} state. However, to our initial surprise, the two main hydride bands for the enzyme spectra are upshifted vs those observed for $[2^{57}Fe\text{-ODT}]_H$-*Cr*HydA1 (Figure S3).[21] For both proteins, the $[2^{57}Fe\text{-ODT}]_H$ 670 cm^{-1} band is upshifted by 5 cm^{-1} to 675 cm^{-1}, while the $[2^{57}Fe\text{-ODT}]_H$ 727 cm^{-1} band upshifts by 17/20 cm^{-1} to 744/747 cm^{-1} for $[2^{57}Fe]_H$-

DOI: 10.1021/jacs.7b09751
J. Am. Chem. Soc. 2017, 139, 16894−16902

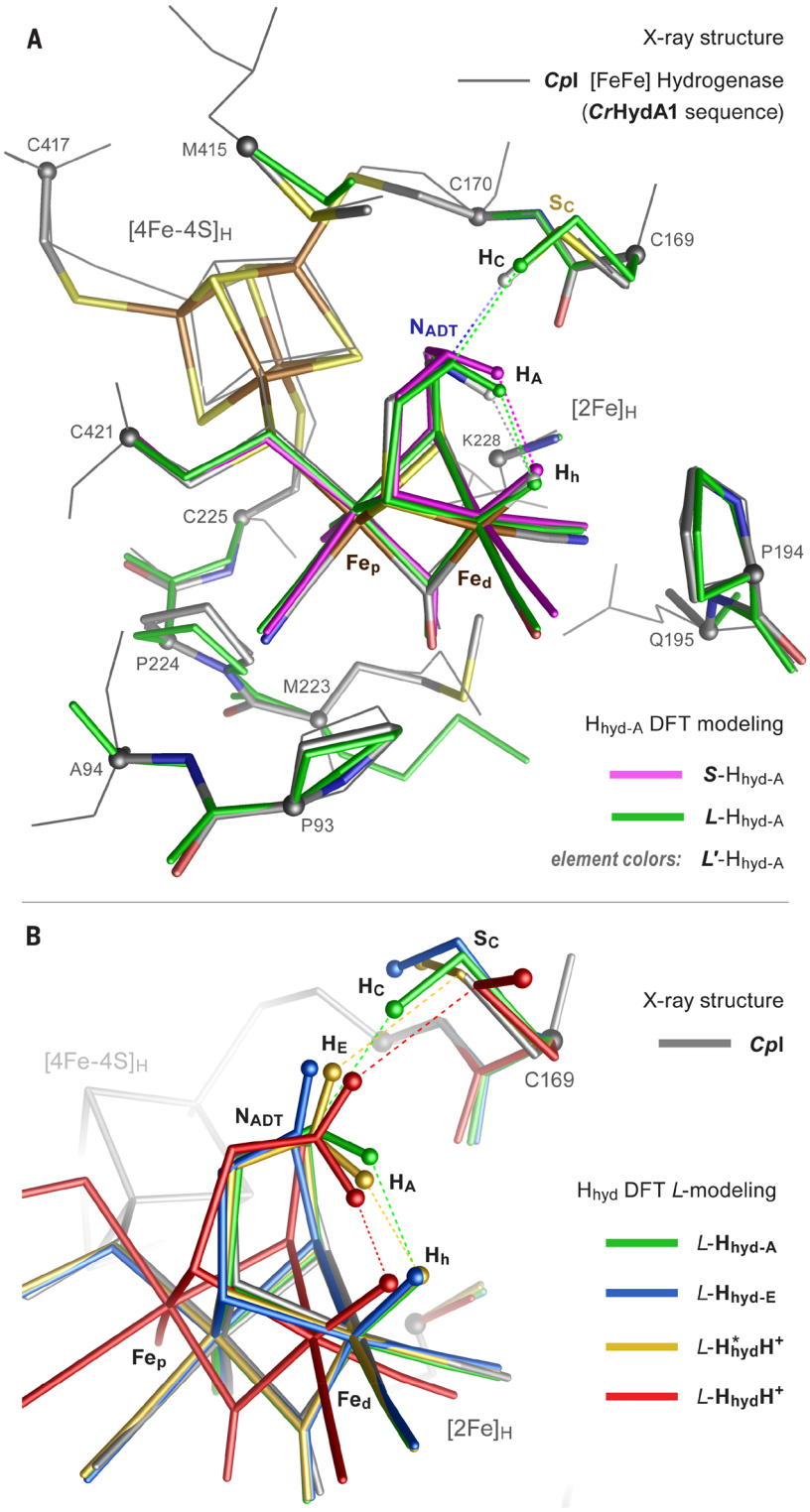

Figure 4. DFT modeling of the H_{hyd} state alternatives. (A) The best-fit $H_{hyd\text{-}A}$ state optimized at three different modeling levels *S* (purple tubes), *L* (green tubes) and *L′* (tubes in element colors) (see Supporting Information), overlaid with the X-ray crystal structure[30] of the *Cp*I [FeFe]-hydrogenase (gray wire frame). All protons except the mechanistically central protons (H_h, H_A and H_C) are omitted for clarity. The same structures with all protons included are shown in Figure S4. (B) Close view of the alternative H_{hyd} configurations $H_{hyd\text{-}A}$ (green), $H_{hyd\text{-}E}$ (blue), $H^*_{hyd}H^+$ (yellow) and $H_{hyd}H^+$ (red) from *L* modeling, overlaid with the X-ray crystal structure (gray). Dashed lines indicate interatomic interactions $H_h\cdots H_A$, $N_{ADT}\cdots H_C$, and $S_C\cdots H_E$ within 3 Å as detailed in Table S3. For the complete *L* models view, see Figure S6.

*Cr*HydA1/*Dd*HydAB. The obvious question: why should changing N for O in the bridgehead atom, which is at a nonbonding distance of >3 Å from the Fe_d, yield such significantly different shifts in the Fe−H bending mode vibrational frequencies?

DFT Calculations. Although several X-ray crystal structures are available for [FeFe]-hydrogenases,[14,30,31] structural studies

DOI: 10.1021/jacs.7b09751
J. Am. Chem. Soc. 2017, 139, 16894−16902

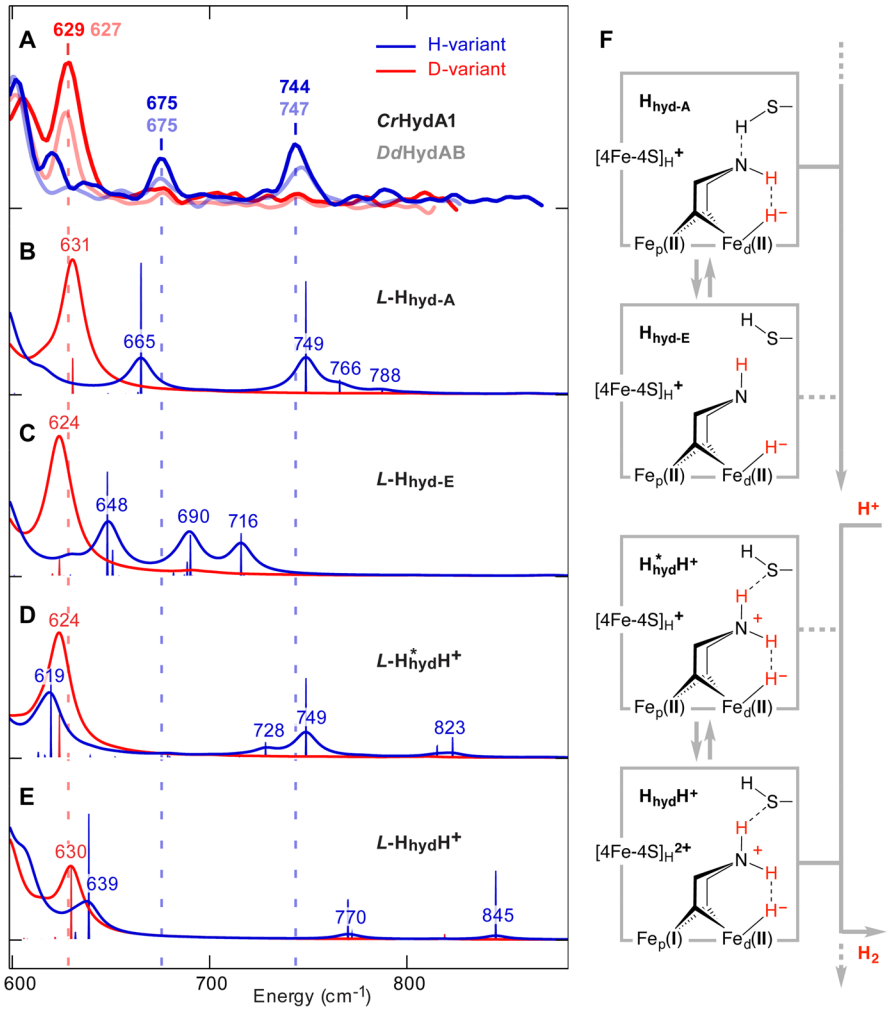

Figure 5. NRVS spectra in the 600−900 cm^{-1} "active window" region (A) for $[2^{57}Fe]_H$-*Cr*HydA1/*Dd*HydAB compared with spectra for the states (B) $H_{hyd\text{-}A}$, (C) $H_{hyd\text{-}E}$, (D) $H^*_{hyd}H^+$ and (E) $H_{hyd}H^+$ simulated using *L* modeling. Blue spectra are for the H-variants and red spectra are for the D-variants. Stick-style peaks in (B−E) are H_h/D_h-PVDOS (partial vibrational density of states) spectra that quantify the hydride-only contribution to the computed vibrational modes. The vertical dotted lines indicate the main peak positions in the observed NRVS spectra. The right panel (F) shows a schematic view of the H_{hyd} variants, placed into the context of the [FeFe]-hydrogenase mechanism.

are lacking for the enzyme with a bound hydride. Four schematic alternatives on H_{hyd} based on earlier proposals[21] are shown in Figure 5F. Two of them, designated $H_{hyd\text{-}A}$ and $H_{hyd\text{-}E}$, assume an uncharged bridgehead amino group, in either "axial" $-N_{ADT}H_A-$ (H_A pointing toward Fe_d) or "equatorial" $-N_{ADT}H_E-$ (H_E pointing away from Fe_d) conformation. The other two alternatives $H^*_{hyd}H^+$ and $H_{hyd}H^+$ assumed a protonated $-N_{ADT}H_2^+-$ form wherein both $H_{A/E}$ locations are occupied, and the $[4Fe\text{-}4S]_H-[2Fe]_H$ subclusters in either $[4Fe\text{-}4S]^+-Fe_p(II)Fe_d(II)$ or $[4Fe\text{-}4S]^{2+}-Fe_p(I)Fe_d(II)$ oxidation levels.

DFT modeling of the H_{hyd} state, therefore, provides insight into the conformation and the protonation state of the bridging ADT ligand, as well as the electronic configuration at the Fe sites. We started our analysis at a "*Small*" DFT modeling level called *S*, including only the $[2Fe]_H$ subcluster and the Cys421/382 side chain that coordinates Fe_p (see Figures 4A, S4, and S5, Tables S1 and S2, and Supplementary Discussion in Supporting Information for details on the DFT modeling); earlier, this type of modeling has been applied to rationalize the NRVS Fe−H bands in $[2^{57}Fe\text{-ODT}]_H$-*Cr*HydA1.[21] As shown in Figure S10, the *S* modeling of the four H_{hyd} states produced a significantly variable distribution of the Fe_d-H_h bands. Only *S*-$H_{hyd\text{-}A}$ with its Fe_d-H_h modes at 668 and 764 cm^{-1} satisfactorily simulated the observed spread and relative intensities of the two NRVS bands. The "*Small*" DFT models were thus useful for distinguishing the major protonation and conformational alternatives.

It is well-known, however, that the $[4Fe\text{-}4S]_H$ subcluster and the protein environment surrounding the H-cluster play crucial roles in the enzyme's properties,[16] and H-bonding between ADT protons and the neighboring Cys169/178 residue are also important. We, therefore, proceeded to explore the four H_{hyd} alternatives using a "*Large*" modeling level *L* that, beyond *S*, integrated protein side chains surrounding the $[2Fe]_H$ subcluster (see Figures 4A and B, S4 and S6). A second large model, labeled *L*′ and additionally included the $[4Fe\text{-}4S]_H$ subcluster, was evaluated (see Figure S7).

The 600−900 cm^{-1} "active window" is uniquely sensitive to Fe−H/D bending motions. As shown in Figure 5A−E, model *L*-$H_{hyd\text{-}A}$ is the only simulation that reasonably replicates the positions and intensities of the two observed Fe−H bands. The other *L*-H_{hyd} models predict either too many bands (*L*-$H_{hyd\text{-}E}$), only a single band (*L*-$H^*_{hyd}H^+$), or hardly any bands

DOI: 10.1021/jacs.7b09751
J. Am. Chem. Soc. 2017, 139, 16894−16902

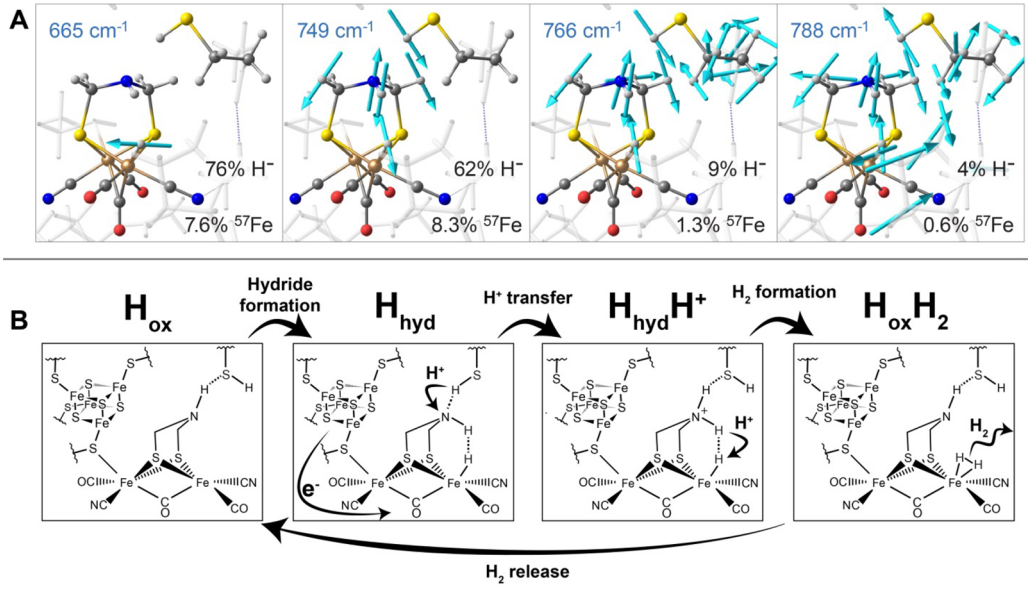

Figure 6. DFT-calculated normal modes and possible mechanism of H_2 formation in [FeFe]-hydrogenase. (A) The unscaled arrow representation of relevant atoms motion in the normal modes at 665, 749, 766, and 788 cm^{-1} for model *L*-$H_{hyd\text{-}A}$ (cf. Figure 5B). Contributions from the H_h and ^{57}Fe nuclei to the vibrational energies are given. (B) Proposed sequence of events leading to H_2 formation: H_{hyd} becomes protonated leading to $H_{hyd}H^+$, and subsequently bond formation occurs giving the H_2 product complex. H_2 release generates the H_{ox} state of the enzyme, which can be reduced and protonated to form H_{hyd} again.

(*L*-$H_{hyd}H^+$), with intensity levels above the experimental noise. Interestingly, the total intensity concentrated in the calculated Fe_d–H_h bands decreases in the sequence $H_{hyd\text{-}E}$ > $H_{hyd\text{-}A}$ > $H^*_{hyd}H^+$ > $H_{hyd}H^+$, which correlates with the strength of the ADT-hydride interaction, as reflected by the $H_h\cdots H_A$ distances collected in Table S3. Only for the $H_{hyd\text{-}E}$ alternative that lacks the H_A proton, modeling *S* and *L* predict essentially the same set of Fe_d–H_h bands (Figure S10C). For other H_{hyd} alternatives the $H_h\cdots H_A$ hydride interaction with ADT is communicated further to Cys169/178 only in the *L* models, and *S* vs *L* band positions generally diverge (Figure S10B,D,E). For the best-fit hydride state, inclusion of Cys169/178 in the *L*-$H_{hyd\text{-}A}$ model leads to an improvement in the higher frequency Fe_d–H_h mode position by 15 cm^{-1} (764 in *S*-$H_{hyd\text{-}A}$ and 749 in *L*-$H_{hyd\text{-}A}$, vs 744/749 cm^{-1} observed, see Figure S10B). We note also that our preference for $H_{hyd\text{-}A}$ is supported by its ≈6–9 kcal/mol lower energy vs $H_{hyd\text{-}E}$ (Table S5). Simulations for the entire spectral range reported in Figures S9 and S11–S14 provide additional support for $H_{hyd\text{-}A}$, and unequivocally indicate the benefits of the large DFT models for reproducing NRVS bands <400 cm^{-1}.

The motion of the various nuclei that is the source of the calculated intensities for the *L*-$H_{hyd\text{-}A}$ bands (Figure 5B) are illustrated in Figure 6A and animated vibrational modes available in Supporting Information. The mode calculated at 665 cm^{-1} and associated with the band observed at 675 cm^{-1} involves essentially pure H_h motion normal to the $Fe_pFe_dH_h$ plane. In contrast, the three higher frequency modes are in-plane H_h motions becoming increasingly less pure and more strongly coupled to the ADT bridgehead, Cys169/178, and further molecular fragments. The in-plane modes can be characterized in terms of in/out of phase motion of the hydride, ADT, and cysteine H nuclei: [H_h↓H_A↓H_C↓] at 749, [H_h↑H_A↓H_C↓] at 766, and [H_h↑H_A↓H_C↑] at 788 cm^{-1}. Among the in-plane modes, only the one at 749 cm^{-1} has sufficient ^{57}Fe motion to be detected in the NRVS experiment and associated with the H_{hyd} band observed at 744/747 cm^{-1}. Transition from the *S* to *L* modeling for the $H_{hyd\text{-}A}$ spectral simulations reveals that the *intrinsically* decoupled out-of-plane hydride mode hardly changes its position (Figure S10B, 668 to 665 cm^{-1}) upon the protein environment inclusion. In contrast, the coupled in-plane mode shifts by −15 cm^{-1} as discussed above. Here, *S* vs *L* modeling replicates the behavior of the [2^{57}Fe-ODT]$_H$ vs [2^{57}Fe]$_H$ protein systems on the two Fe–H band shifts (see the NRVS section above); only in the [2^{57}Fe]$_H$ systems the $H_h\cdots H_A$ interaction is present, and the higher energy Fe_d–H_h mode becomes delocalized.

Mechanistic Proposal. The details of the catalytic mechanism of [FeFe]-hydrogenases have been debated for decades.[1,8,11,12,35] Past proposals for the catalytic mechanism can be divided into one set involving a bridging hydride between Fe_p and Fe_d[36] (Mechanism I as described by Trohalaki and Pachter[11]) and another set involving a terminal hydride on Fe_d (Mechanism II).[35] We see no evidence that H_{hyd} involves a bridging hydride. Notably, in contrast to the [2^{57}Fe]$_H$-*Cr*HydA1/*Dd*HydAB samples and the best-fit $H_{hyd\text{-}A}$ state producing *two* (Fe–H bending) bands in the NRVS "active window" (Figure 5A and B), bridging Ni(II)(*μ*-H)^{57}Fe(II) hydrides in [NiFe]-hydrogenase and a model complex produced only a *single* (Ni–H–Fe wagging) band.[37] A qualitatively similar result displaying strong deviations to the observed H_{hyd} spectra is obtained from a $^{57}Fe_p$(II)(*μ*-H)$^{57}Fe_d$(II) DFT candidate called *L*-$H_{\mu\text{-}hyd\text{-}A}$ (see Figures S8 and S15, and Supplementary Discussion in Supporting Information). Other reports also disfavor bridging hydride-based mechanisms on a variety of grounds.[12,38] We thus consider the implications of the NRVS results on mechanisms involving a terminal hydride. For this case, a consensus has emerged that proton transfer from an $-NH_2^+-$ form of the bridgehead nitrogen to Fe_d hydride is the key step in H_2 formation.

DOI: 10.1021/jacs.7b09751
J. Am. Chem. Soc. 2017, 139, 16894–16902

We note that model L-$H_{hyd\text{-}A}$ predicts a $H_h\cdots H_A$ distance of 2.01 Å (Table S3), a similar Fe−H···H−N distance of 1.88 Å observed in the $[(H)Fe_2(adt\text{-}NH_2)(CO)_2(dppv)_2](BF_4)_2$ complex by X-ray crystallography.[9] This distance is still quite a bit longer than the ≈1.5 Å H···H distance reported by Bullock and co-workers for a strong Fe−H···H−N dihydrogen interaction.[10] The long Fe−H···H−N distance in the complex is, however, a consequence of hydrogen bonding to the BF_4^- anion.[39] Therefore, model L-$H_{hyd\text{-}A}$ probably represents motions of the nuclei related to a step prior to the last step leading to H_2 formation. H_2 production from state $H_{hyd\text{-}A}$ requires transfer of the amino proton to subsequently yield an Fe_d−H_2 complex (see Figure 6B). This process requires assistance from the proton transport chain, either to first produce $-NH_2^+-$ (or to transfer H^+ in a concerted mechanism). DFT modeling L' including both $[2Fe]_H$ and $[4Fe\text{-}4S]_H$ subclusters indicates that protonation of $H_{hyd\text{-}A}$ yields an $[4Fe\text{-}4S]^{2+}$−$Fe_p(I)Fe_d(II)$ species $H_{hyd}H^+$, and the $[4Fe\text{-}4S]^+$−$Fe_p(II)Fe_d(II)$ alternative $H^*_{hyd}H^+$ is disfavored (see Figure 5F, Table S4, and Supplementary Discussion in Supporting Information).

For the next step, Bullock and co-workers have proposed that $-NH_2^+-$/Fe−H and −NH−/Fe−H_2 species exist in rapid equilibrium, both in their model complex and in [FeFe]-hydrogenases.[10] Our calculations for model L-$H_{hyd}H^+$, which posits an $Fe_p(I)Fe_d(II)$ redox level and $-NH_2^+-$/Fe−H coordination, finds an $H_h\cdots H_A$ distance of 1.38 Å (Table S3), even shorter than in the Bullock complex, and it is thus reasonable that a similar $-NH_2^+-$/Fe−H ⇄ −NH−/Fe−H_2 equilibrium would occur. We propose that protonation of $H_{hyd\text{-}A}$, in concert with electron transfer from $[4Fe\text{-}4S]_H$ to $[2Fe]_H$, yields $H_{hyd}H^+$, which can directly yield an Fe−H_2 species. Capturing this dihydrogen complex experimentally is an excellent target for future studies.

CONCLUSIONS

The key hydride intermediate in [FeFe]-hydrogenase catalysis has been directly identified for the first time in two native enzymes using selective vibrational spectroscopy. The NRVS vibrational data are consistent with a terminal hydride at the distal iron of the $[2Fe]_H$ subsite interacting with the amine proton of the azaditholate cofactor. As indicated by the diversity of the DFT-simulated spectra, the Fe_d−H_h center in the [FeFe]-hydrogenases is exquisitely sensitive to its environment. The protonation states of the amine and its interaction with the cysteine residue at the end of the proton supply chain, as well as the redox levels of the $[2Fe]_H$ and $[4Fe\text{-}4S]_H$ subclusters are shown to strongly influence the Fe_d−H_h bending vibrations. Rationalized by theory, distinctive ^{57}Fe−H/D spectroscopic signatures from NRVS are, therefore, anticipated to be diagnostic in other Fe-containing enzymes and molecular models. Although iron hydrides have been detected previously in variants of the [FeFe]-hydrogenases, the present work gives the first structure for the enzyme−substrate complex in a catalytically competent state. Furthermore, the structure of this hydride intermediate paints a coherent picture for the sequence of events leading to evolution of H_2.

METHODS

Sample Preparation. $[2^{57}Fe]_H$-*Cr*HydA1 and $[2^{57}Fe]_H$-*Dd*HydAB were prepared as described previously,[27,40] but using an ^{57}Fe-labeled azadithiolate cofactor.[25] All sample preparation steps were performed in an anaerobic glovebox (Coy) under 2% H_2 (or D_2)/98% N_2. Samples of $[2^{57}Fe]_H$-*Cr*HydA1 (60 μL of 3−5 mM) in pH 6 buffer (50 mM MES, 50 mM HEPES, 150 mM NaCl, either in H_2O or D_2O) and $[2^{57}Fe]_H$-*Dd*HydAB (60 μL of 2−4 mM) in pH 4 buffer (100 mM sodium acetate, 150 mM NaCl, either in H_2O or D_2O) were reduced with 100 mM sodium dithionite, 50 μL were transferred to each NRVS cell and frozen in liquid nitrogen, and the remaining 10 μL were loaded into an FTIR cell and measured within 5 min.

Fourier-Transform Infrared Spectroscopy. FTIR spectra were collected using a Bruker IFS 66v/S FT-IR spectrometer equipped with a liquid nitrogen cooled Bruker mercury cadmium telluride (MCT) detector. Measurements were performed at room temperature in the double-sided, forward−backward mode with a resolution of 2 cm^{-1}, an aperture setting of 1.5 mm and a scan velocity of 20 Hz. Data were processed using home-written routines in the MATLAB platform.

Nuclear Resonance Vibrational Spectroscopy. NRVS spectra for $[2^{57}Fe]_H$-*Cr*HydA1 and $[2^{57}Fe]_H$-*Dd*HydAB were recorded at SPring-8 BL09XU[41] and BL19LXU.[42] BL09XU uses a Si(111) double crystal in a high heat load monochromator (HHLM) to produce 14.414 keV radiation with ≈1.0 eV resolution, followed by a high energy resolution monochromator (HRM) [Ge(422) × 2Si(975)] to increase the resolution to 0.8 meV. The beam flux was ∼2.5 × 10^9 photons/s and the beam size was about 0.6 (height) × 1 (width) mm^2. A 2 × 2 avalanche photodiode (APD) detector array was used to collect the delayed nuclear fluorescence and the K_α fluorescence following nuclear excitation. The temperature at the base of the sample was maintained at 10 K with a LHe cryostat. The Stoke/anti-Stoke imbalance derived real sample temperatures were 40−70 K.[43]

BL19LXU[42] provides the fundamental beam at 7.2−18 keV energy region, covering ^{57}Fe nuclear resonance at 14.414 keV. Its 25-m undulator produces about 5x higher beam flux at HHLM than that at BL09XU. Therefore, it is a good choice for NRVS measurements on weak vibrational features, such as ^{57}Fe-H/D. BL19LXU is not a dedicated nuclear scattering beamline, and a similar HMR and associated NRVS measurement system was integrated into the BL19LXU's experimental hutch during the first 36−48 h of each beamtime. Therefore, BL19LXU provided 14.414 keV radiation with 0.8 meV resolution, with an average photon flux of ∼5.4 × 10^9 photons/s. The beam size was also 0.6 × 1 mm^2. The delayed signal was also measured with a 2 × 2 APD array. The real sample temperatures were also 40−70 K.

NRVS spectral analysis was performed using the PHOENIX software package[44] executed through spectra.tools.[45] The energy scales were calibrated with a standard sample of $[NEt_4][^{57}FeCl_4]$ with a prominent peak at 380 cm^{-1}.

Since the relative strength of NRVS transitions varies dramatically and since it is necessary to emphasize one region of interest (e.g., for searching for Fe−H−Fe or X−Fe-H), the scans were divided into segments with different data collection times (second per point, or s/p). In general, 1 s/p was used for the range from −240 to 400 cm^{-1} (covering the Fe−S region), then 5−10 s/p. for the Fe−CN and Fe−CO region from 400 to 620 cm^{-1}. A longer scanning time (16−23 s) was used for the Fe−H or X−Fe−H region (e.g., at 640−800 cm^{-1}). The scan ranges are all relative about the resonance energy.

DFT Calculations. The density functional theory (DFT) methodology presently applied to the [FeFe]-hydrogenase H-cluster modeling is mostly equivalent to that employed earlier.[21] The structural optimizations and subsequent normal mode calculations were performed using GAUSSIAN 09 Revision D.01[46] based on the densities exported from single point calculations performed by JAGUAR 9.4[47] that provided high-quality initial guess. The BP86[48,49] functional and the LACV3P** basis set as implemented in JAGUAR were employed, unless otherwise mentioned. For the first- and second-row elements, LACV3P** implies 6-311G** triple-ζ basis sets including polarization functions. For the Fe atoms, LACV3P** consists of a triple-ζ basis set for the outermost core and valence orbitals, and the quasi-relativistic Los Alamos effective core potential (ECP) for the innermost electrons. The molecular systems environment was considered using a self-consistent reaction field (SCRF) polarizable continuum model and integral equation formalism (IEF-PCM)[50] as implemented in GAUSSIAN 09, with the static dielectric

DOI: 10.1021/jacs.7b09751
J. Am. Chem. Soc. 2017, 139, 16894−16902

constant set to $\varepsilon = 4.0$ as often used for proteins, and the remaining IEF-PCM parameters at their default values for water.

Our attempts to vary the DFT methodology described above using alternative functionals (specifically nonhybrid PBE,[51] hybrid PBE0,[52] and hybrid B3LYP[53−56] including variations on the exact exchange admixture) did not produce any better correspondence between the DFT-calculated and NRVS-observed vibrational data. When applicable, the B3LYP functional results are for single-point calculations only.

Computational schemes were furthermore tested (i) excluding and (ii) including two-body D3 empirical dispersion correction by Grimme et al. in its original formulation,[57] as well as (iii) D3 reformulated with Becke−Johnson damping.[58] Optimal results for reproducing the observed NRVS spectra were found from using scheme (i) for modeling levels S and $L > 400$ cm^{-1}, and from using scheme (ii) for modeling level $L' < 400$ cm^{-1}; the H-cluster modeling levels $S/L/L'$ are explained in section "Model Setup" of the Supporting Information and Table S1, and shown in Figures 4A and S4.

DFT Spectra Simulation. DFT-based vibrational data (Figures 5B-E, S9−S15) were generated using selective $[2^{57}\mathrm{Fe}]_{\mathrm{H}}$ subcluster labeling as employed in the NRVS experiment. Simulation of the deuterated samples, referred in the text as "D-variants", introduced additional H-to-D substitutions applied to hydrogen nuclei labeled as $H_h/H_A/H_E/H_C$ throughout the manuscript. The ^{57}Fe-PVDOS and hydride-only H^-/D^--PVDOS intensities were extracted from normal mode outputs using an in-house Q-SPECTOR program, successfully applied earlier.[21,37,59−63] To account for the resolution of the present NRVS experiment, computed ^{57}Fe-PVDOS intensities were broadened by convolution with a full width at half-maximum (fwhm) = 14 cm^{-1} Lorentzian. Homogeneous empirical scaling of the calculated frequencies by 96% was applied to modeling levels S and L, and no frequency scaling has been applied (100%) to modeling level L'. On the basis of the approach described in Supplementary Discussion of the Supporting Information, the representative full-range spectra (Figures S9, S11−S14) combined ^{57}Fe-PVDOS from modeling levels $L > 400$ cm^{-1} and $L' < 400$ cm^{-1} and referred to as "L-modeling". This combined approach provided essentially unambiguous mapping between the ^{57}Fe-PVDOS features observed for the protein samples and calculated for the best-fit state $H_{hyd\text{-}A}$.

■ ASSOCIATED CONTENT

Supporting Information

The Supporting Information is available free of charge on the ACS Publications website at DOI: 10.1021/jacs.7b09751.

Supplementary FTIR, EPR, Mössbauer, NRVS, and DFT figures and tables; Supplementary Discussion on the DFT models (PDF)

Coordinates of the DFT models as XYZ files (ZIP)

Animated vibrational normal modes as GIF files (ZIP)

■ AUTHOR INFORMATION

Corresponding Author

*spjcramer@ucdavis.edu

ORCID

Thomas B. Rauchfuss: 0000-0003-2547-5128

Wolfgang Lubitz: 0000-0001-7059-5327

Author Contributions

[#]V.P., J.A.B., C.C.P. contributed equally to this work.

Notes

The authors declare no competing financial interest.

■ ACKNOWLEDGMENTS

This work was supported by NIH GM-65440 (S.P.C.), NIH GM-GM-61153 (T.B.R.), the Cluster of Excellence "Unifying Concepts in Catalysis" initiative of DFG (V.P.), and the Max Planck Society. NRVS data collection was supported by the following proposals to SPring-8: [2015B1134], [2016B1347], [2016A1154], long term proposals at BLXU09: [2015A0103], [2015B0103], [2016A0103], and long-term proposals at BLXU19: [20140033], [20150048], [20160063]. The authors thank Bernd Mienert for Mössbauer sample measurements and Patricia Malkowski and Nina Breuer for technical assistance.

■ REFERENCES

(1) Lubitz, W.; Ogata, H.; Rüdiger, O.; Reijerse, E. *Chem. Rev.* **2014**, *114*, 4081.

(2) Peters, J. W.; Schut, G. J.; Boyd, E. S.; Mulder, D. W.; Shepard, E. M.; Broderick, J. B.; King, P. W.; Adams, M. W. W. *Biochim. Biophys. Acta, Mol. Cell Res.* **2015**, *1853*, 1350.

(3) Hatchikian, E. C.; Magro, V.; Forget, N.; Nicolet, Y.; Fontecilla-Camps, J. C. *J. Bact.* **1999**, *181*, 2947.

(4) Silakov, A.; Wenk, B.; Reijerse, E.; Lubitz, W. *Phys. Chem. Chem. Phys.* **2009**, *11*, 6592.

(5) Carr, S. B.; Evans, R. M.; Brooke, E. J.; Wehlin, S. A. M.; Nomerotskaia, E.; Sargent, F.; Armstrong, F. A.; Phillips, S. E. V. *Biochem. Soc. Trans.* **2016**, *44*, 863.

(6) Kalz, K. F.; Brinkmeier, A.; Dechert, S.; Mata, R. A.; Meyer, F. *J. Am. Chem. Soc.* **2014**, *136*, 16626.

(7) Mulder, D. W.; Ratzloff, M. W.; Bruschi, M.; Greco, C.; Koonce, E.; Peters, J. W.; King, P. W. *J. Am. Chem. Soc.* **2014**, *136*, 15394.

(8) Schilter, D.; Camara, J. M.; Huynh, M. T.; Hammes-Schiffer, S.; Rauchfuss, T. B. *Chem. Rev.* **2016**, *116*, 8693.

(9) Carroll, M. E.; Barton, B. E.; Rauchfuss, T. B.; Carroll, P. J. *J. Am. Chem. Soc.* **2012**, *134*, 18843.

(10) Liu, T. B.; Wang, X. P.; Hoffmann, C.; DuBois, D. L.; Bullock, R. M. *Angew. Chem., Int. Ed.* **2014**, *53*, 5300.

(11) Trohalaki, S.; Pachter, R. *Int. J. Hydrogen Energy* **2010**, *35*, 5318.

(12) Finkelmann, A. R.; Stiebritz, M. T.; Reiher, M. *Chem. Sci.* **2014**, *5*, 215.

(13) Yang, Z.; Lasker, K.; Schneidman-Duhovny, D.; Webb, B.; Huang, C. C.; Pettersen, E. F.; Goddard, T. D.; Meng, E. C.; Sali, A.; Ferrin, T. E. *J. Struct. Biol.* **2012**, *179*, 269.

(14) Nicolet, Y.; Piras, C.; Legrand, P.; Hatchikian, C. E.; Fontecilla-Camps, J. C. *Structure* **1999**, *7*, 13.

(15) Hong, G.; Cornish, A. J.; Hegg, E. L.; Pachter, R. *Biochim. Biophys. Acta, Bioenerg.* **2011**, *1807*, 510.

(16) Knörzer, P.; Silakov, A.; Foster, C. E.; Armstrong, F. A.; Lubitz, W.; Happe, T. *J. Biol. Chem.* **2012**, *287*, 1489.

(17) Das, R.; Neese, F.; van Gastel, M. *Phys. Chem. Chem. Phys.* **2016**, *18*, 24681.

(18) Morra, S.; Giraudo, A.; Di Nardo, G.; King, P. W.; Gilardi, G.; Valetti, F. *PLoS One* **2012**, *7*, e48400.

(19) Siebel, J. F.; Adamska-Venkatesh, A.; Weber, K.; Rumpel, S.; Reijerse, E.; Lubitz, W. *Biochemistry* **2015**, *54*, 1474.

(20) Tal, S.; Chun, T. W.; Gavini, N.; Burgess, B. K. *J. Biol. Chem.* **1991**, *266*, 10654.

(21) Reijerse, E. J.; Pham, C. C.; Pelmenschikov, V.; Gilbert-Wilson, R.; Adamska-Venkatesh, A.; Siebel, J. F.; Gee, L. B.; Yoda, Y.; Tamasaku, K.; Lubitz, W.; Rauchfuss, T. B.; Cramer, S. P. *J. Am. Chem. Soc.* **2017**, *139*, 4306.

(22) Wang, H.; Alp, E. E.; Yoda, Y.; Cramer, S. P. *Methods Mol. Biol.* **2014**, *1122*, 125.

(23) Scheidt, W. R.; Durbin, S. M.; Sage, J. T. *J. Inorg. Biochem.* **2005**, *99*, 60.

(24) Seto, M.; Yoda, Y.; Kikuta, S.; Zhang, X. W.; Ando, M. *Phys. Rev. Lett.* **1995**, *74*, 3828.

(25) Gilbert-Wilson, R.; Siebel, J. F.; Pham, C. C.; Adamska-Venkatesh, A.; Reijerse, E.; Wang, H.; Cramer, S. P.; Lubitz, W.; Rauchfuss, T. B. *J. Am. Chem. Soc.* **2015**, *137*, 8998.

(26) Berggren, G.; Adamska, A.; Lambertz, C.; Simmons, T. R.; Esselborn, J.; Atta, M.; Gambarelli, S.; Mouesca, J. M.; Reijerse, E.; Lubitz, W.; Happe, T.; Artero, V.; Fontecave, M. *Nature* **2013**, *499*, 66.

(27) Esselborn, J.; Lambertz, C.; Adamska-Venkatesh, A.; Simmons, T.; Berggren, G.; Nothl, J.; Siebel, J.; Hemschemeier, A.; Artero, V.; Reijerse, E.; Fontecave, M.; Lubitz, W.; Happe, T. *Nat. Chem. Biol.* **2013**, *9*, 607.
(28) Mulder, D. W.; Guo, Y.; Ratzloff, M. W.; King, P. W. *J. Am. Chem. Soc.* **2017**, *139*, 83.
(29) Winkler, M.; S, M.; Duan, J.; Esselborn, J.; Wittkamp, F.; Hofmann, E.; Apfel, U. P.; Stripp, S. T.; Happe, T. *Nat. Commun.* **2017**, *8*, 16115.
(30) Esselborn, J.; Muraki, N.; Klein, K.; Engelbrecht, V.; Metzler-Nolte, N.; Apfel, U. P.; Hofmann, E.; Kurisu, G.; Happe, T. *Chem. Sci.* **2016**, *7*, 959.
(31) Peters, J. W.; Lanzilotta, W. N.; Lemon, B. J.; Seefeldt, L. C. *Science* **1998**, *282*, 1853.
(32) Glick, B. R.; Martin, W. G.; Martin, S. M. *Can. J. Microbiol.* **1980**, *26*, 1214.
(33) Happe, T.; Naber, J. D. *Eur. J. Biochem.* **1993**, *214*, 475.
(34) Senger, M.; Mebs, S.; Duan, J.; Shulenina, O.; Laun, K.; Kertess, L.; Wittkamp, F.; Apfel, U. P.; Happe, T.; Winkler, M.; Haumann, M.; Stripp, S. T. *Phys. Chem. Chem. Phys.* **2018**, DOI: 10.1039/C7CP04757F.
(35) Siegbahn, P. E. M.; Tye, J. W.; Hall, M. B. *Chem. Rev.* **2007**, *107*, 4414−4435.
(36) Zhou, T. J.; Mo, Y. R.; Liu, A. M.; Zhou, Z. H.; Tsai, K. R. *Inorg. Chem.* **2004**, *43*, 923.
(37) Ogata, H.; Kraemer, T.; Wang, H.; Schilter, D.; Pelmenschikov, V.; van Gastel, M.; Neese, F.; Rauchfuss, T. B.; Gee, L. B.; Scott, A. D.; Yoda, Y.; Tanaka, Y.; Lubitz, W.; Cramer, S. P. *Nat. Commun.* **2015**, *6*, 7890.
(38) Mebs, S.; Senger, M.; Duan, J.; Wittkamp, F.; Apfel, U.-P.; Happe, T.; Winkler, M.; Stripp, S. T.; Haumann, M. *J. Am. Chem. Soc.* **2017**, *139*, 12157.
(39) Huynh, M. T.; Wang, W.; Rauchfuss, T. B.; Hammes-Schiffer, S. *Inorg. Chem.* **2014**, *53*, 10301.
(40) Birrell, J. A.; Wrede, K.; Pawlak, K.; Rodriguez-Maciá, P.; Rüdiger, O.; Reijerse, E. J.; Lubitz, W. *Isr. J. Chem.* **2016**, *56*, 852.
(41) Yoda, Y.; Yabashi, M.; Izumi, K.; Zhang, X. W.; Kishimoto, S.; Kitao, S.; Seto, M.; Mitsui, T.; Harami, T.; Imai, Y.; Kikuta, S. *Nucl. Instrum. Methods Phys. Res., Sect. A* **2001**, *467*, 715.
(42) Yabashi, M.; Tamasaku, K.; Kikuta, S.; Ishikawa, T. *Rev. Sci. Instrum.* **2001**, *72*, 4080.
(43) Wang, H. X.; Yoda, Y.; Kamali, S.; Zhou, Z. H.; Cramer, S. P. *J. Synchrotron Radiat.* **2012**, *19*, 257.
(44) Sturhahn, W.; Toellner, T. S.; Alp, E. E.; Zhang, X.; Ando, M.; Yoda, Y.; Kikuta, S.; Seto, M.; Kimball, C. W.; Dabrowski, B. *Phys. Rev. Lett.* **1995**, *74*, 3832.
(45) Crouthers, D. J.; Ding, S. D.; Denny, J. A.; Bethel, R. D.; Hsieh, C. H.; Hall, M. B.; Darensbourg, M. Y. *Angew. Chem., Int. Ed.* **2015**, *54*, 11102.
(46) Frisch, M. J.; Trucks, G. W.; Schlegel, H. B.; Scuseria, G. E.; Robb, M. A.; Cheeseman, J. R.; Scalmani, G.; Barone, V.; Mennucci, B.; Petersson, G. A.; Nakatsuji, H.; Caricato, M.; Li, X.; Hratchian, H. P.; Izmaylov, A. F.; Bloino, J.; Zheng, G.; Sonnenberg, J. L.; Hada, M.; Ehara, M.; Toyota, K.; Fukuda, R.; Hasegawa, J.; Ishida, M.; Nakajima, T.; Honda, Y.; Kitao, O.; Nakai, H.; Vreven, T.; Montgomery, J. A., Jr.; Peralta, J. E.; Ogliaro, F.; Bearpark, M.; Heyd, J. J.; Brothers, E.; Kudin, K. N.; Staroverov, V. N.; Kobayashi, R.; Normand, J.; Raghavachari, K.; Rendell, A.; Burant, J. C.; Iyengar, S. S.; Tomasi, J.; Cossi, M.; Rega, N.; Millam, J. M.; Klene, M.; Knox, J. E.; Cross, J. B.; Bakken, V.; Adamo, C.; Jaramillo, J.; Gomperts, R.; Stratmann, R. E.; Yazyev, O.; Austin, A. J.; Cammi, R.; Pomelli, C.; Ochterski, J. W.; Martin, R. L.; Morokuma, K.; Zakrzewski, V. G.; Voth, G. A.; Salvador, P.; Dannenberg, J. J.; Dapprich, S.; Daniels, A. D.; Farkas, Ö.; Foresman, J. B.; Ortiz, J. V.; Cioslowski, J.; Fox, D. J. *Gaussian 09*, Revision D.01; Gaussian Inc.: Wallingford, CT, 2009.
(47) *Jaguar, version 9.4*, Schrodinger, Inc., New York, NY, 2016.
(48) Becke, A. D. *Phys. Rev. A: At., Mol., Opt. Phys.* **1988**, *38*, 3098.
(49) Perdew, J. P. *Phys. Rev. B: Condens. Matter Mater. Phys.* **1986**, *33*, 8822.
(50) Tomasi, J.; Mennucci, B.; Cammi, R. *Chem. Rev.* **2005**, *105*, 2999.
(51) Perdew, J. P.; Burke, K.; Ernzerhof, M. *Phys. Rev. Lett.* **1996**, *77*, 3865.
(52) Adamo, C.; Barone, V. *J. Chem. Phys.* **1999**, *110*, 6158.
(53) Becke, A. D. *J. Chem. Phys.* **1993**, *98*, 5648.
(54) Lee, C. T.; Yang, W. T.; Parr, R. G. *Phys. Rev. B: Condens. Matter Mater. Phys.* **1988**, *37*, 785.
(55) Vosko, S. H.; Wilk, L.; Nusair, M. *Can. J. Phys.* **1980**, *58*, 1200.
(56) Stephens, P. J.; Devlin, F. J.; Chabalowski, C. F.; Frisch, M. J. *J. Phys. Chem.* **1994**, *98*, 11623.
(57) Grimme, S.; Antony, J.; Ehrlich, S.; Krieg, H. *J. Chem. Phys.* **2010**, *132*, 154104.
(58) Grimme, S.; Ehrlich, S.; Goerigk, L. *J. Comput. Chem.* **2011**, *32*, 1456.
(59) Schilter, D.; Pelmenschikov, V.; Wang, H.; Meier, F.; Gee, L. B.; Yoda, Y.; Kaupp, M.; Rauchfuss, T. B.; Cramer, S. P. *Chem. Commun.* **2014**, *50*, 13469.
(60) Mitra, D.; George, S. J.; Guo, Y. S.; Kamali, S.; Keable, S.; Peters, J. W.; Pelmenschikov, V.; Case, D. A.; Cramer, S. P. *J. Am. Chem. Soc.* **2013**, *135*, 2530.
(61) Yan, L. F.; Pelmenschikov, V.; Dapper, C. H.; Scott, A. D.; Newton, W. E.; Cramer, S. P. *Chem. - Eur. J.* **2012**, *18*, 16349.
(62) Pelmenschikov, V.; Guo, Y. S.; Wang, H. X.; Cramer, S. P.; Case, D. A. *Faraday Discuss.* **2011**, *148*, 409.
(63) Mitra, D.; Pelmenschikov, V.; Guo, Y. S.; Case, D. A.; Wang, H. X.; Dong, W. B.; Tan, M. L.; Ichiye, T.; Jenney, F. E.; Adams, M. W. W.; Yoda, Y.; Zhao, J. Y.; Cramer, S. P. *Biochemistry* **2011**, *50*, 5220.

DOI: 10.1021/jacs.7b09751
J. Am. Chem. Soc. 2017, 139, 16894−16902